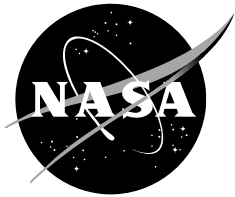# Characterization of Titanium Alloys Produced by Electron Beam Directed Energy Deposition

John A. Newman and Wesley A. Tayon
Langley Research Center, Hampton, Virginia

Timothy J. Ruggles and Saikumar R. Yeratapally
National Institute of Aerospace, Hampton, Virginia

Craig A. Brice
Colorado School of Mines, Golden, Colorado

Jacob D. Hochhalter, James M. Baughman and Harold D. Claytor
Analytical Mechanics Associates, Inc., Hampton, Virginia

NASA STI Program . . . in Profile

Since its founding, NASA has been dedicated to the advancement of aeronautics and space science. The NASA scientific and technical information (STI) program plays a key part in helping NASA maintain this important role.

The NASA STI program operates under the auspices of the Agency Chief Information Officer. It collects, organizes, provides for archiving, and disseminates NASA's STI. The NASA STI program provides access to the NTRS Registered and its public interface, the NASA Technical Reports Server, thus providing one of the largest collections of aeronautical and space science STI in the world. Results are published in both non-NASA channels and by NASA in the NASA STI Report Series, which includes the following report types:

- TECHNICAL PUBLICATION. Reports of completed research or a major significant phase of research that present the results of NASA Programs and include extensive data or theoretical analysis. Includes compilations of significant scientific and technical data and information deemed to be of continuing reference value. NASA counter-part of peer-reviewed formal professional papers but has less stringent limitations on manuscript length and extent of graphic presentations.

- TECHNICAL MEMORANDUM. Scientific and technical findings that are preliminary or of specialized interest, e.g., quick release reports, working papers, and bibliographies that contain minimal annotation. Does not contain extensive analysis.

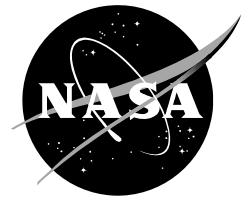- CONTRACTOR REPORT. Scientific and technical findings by NASA-sponsored contractors and grantees.

- CONFERENCE PUBLICATION. Collected papers from scientific and technical conferences, symposia, seminars, or other meetings sponsored or co-sponsored by NASA.

- SPECIAL PUBLICATION. Scientific, technical, or historical information from NASA programs, projects, and missions, often concerned with subjects having substantial public interest.

- TECHNICAL TRANSLATION. English-language translations of foreign scientific and technical material pertinent to NASA's mission.

Specialized services also include organizing and publishing research results, distributing specialized research announcements and feeds, providing information desk and personal search support, and enabling data exchange services.

For more information about the NASA STI program, see the following:

- Access the NASA STI program home page at http://www.sti.nasa.gov

- E-mail your question to help@sti.nasa.gov

- Phone the NASA STI Information Desk at 757-864-9658

- Write to:
  NASA STI Information Desk
  Mail Stop 148
  NASA Langley Research Center
  Hampton, VA 23681-2199

Characterization of Titanium Alloys Produced by Electron Beam Directed Energy Deposition

John A. Newman and Wesley A. Tayon
Langley Research Center, Hampton, Virginia

TimothyJ. Ruggles and Saikumar R. Yeratapally
National Institute of Aerospace, Hampton, Virginia

Craig A. Brice
Colorado School of Mines, Golden, Colorado

Jacob D. Hochhalter, James M. Baughman and Harold D. Claytor
Analytical Mechanics Associates, Inc., Hampton, Virginia

Acknowledgments

Abstract

Functionally graded materials offer the potential to improve structural efficiency by allowing the material composition and/or microstructural features to spatially vary within a component. Additive manufacturing techniques enable the fabrication of such graded materials and structures. While examining several titanium alloys, this paper focuses on Ti-8Al-1Er as it has a unique microstructure that is only feasible when produced by rapid solidification methods like electron beam directed energy deposition, an additive manufacturing process. The results show that, when mixed, Ti-8Al-1Er and commercially-pure titanium uniformly mix at various ratios and the resultant static tensile properties of the mixed alloys behave according to rule-of-mixtures. At discontinuous interfaces between Ti-8Al-1Er and commercially-pure titanium, the crack growth behavior progresses smoothly across the discontinuity as the crack transitions from one crack growth regime into another. Studies on monolithic samples shows the mechanisms of damage in the Ti-8Al-1Er; specifically, that strain localization occurs near grain boundaries of high misorientation on the microscale and that twinning and dislocation density is concentrated near erbia strengthening particles (Er_2O_3) on the nanoscale.

1.   Introduction

Electron beam directed energy deposition (EBDED) is a class of additive manufacturing methods where material is deposited using electron-beam energy [1]. Electron beam freeform fabrication (EBF³) is an emerging EBDED additive manufacturing process that uses an electron beam source to heat an alloy wire feedstock to create a fully-dense, three-dimensional metal structure directly from a computer model [2]. The EBF³ System is manufactured by Sciaky, Inc., Chicago, IL. A schematic of the process is shown in Figure 1. The computer model of the part to be fabricated is first planned as discrete layers, each composed of a series of rows of deposited material. A tool path is generated that can recreate the part from these individual layers and rows. The electron beam is then used to form a molten pool on a substrate plate into which a feedstock wire is fed, thus creating a bead of deposited material. By following the tool path of the deconstructed 3-D object, the EBF³ machine can deposit sequential beads and layers in order to create the part in a freeform manner.
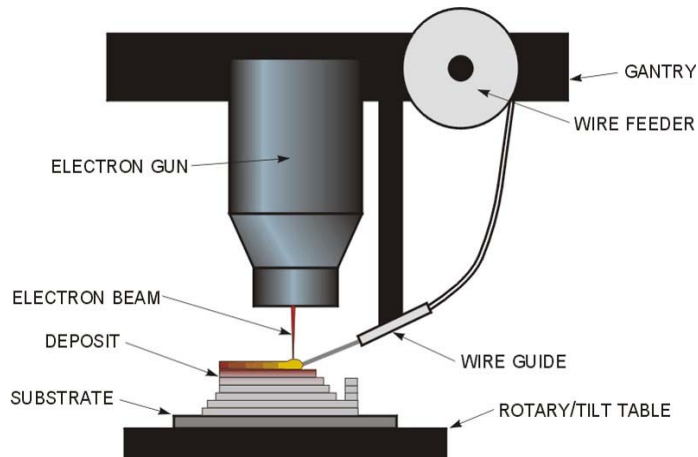

Figure 1. Schematic of EBF³ material production.

A particular advantage of additive manufacturing processes like EBF^3 is the ability to create functional gradient structures through the use of multiple feedstock wires. Thus, within a single component the chemical composition can be locally changed. This could be advantageous for optimizing properties within a given component based on the local design limiting criteria [3]. For example, areas of high toughness could be smoothly transitioned into areas of high strength with the transition determined by the loading conditions within the part. This could greatly increase the structural efficiency of complex structural aerospace components. The objective of this study is to correlate the EBF^3 process with the resulting alloy microstructure and, ultimately, to mechanical performance of titanium alloys.

2. Approach

Several titanium alloys were selected for this study that have different properties, yet are likely still mutually compatible in an EBDED composite product. Of particular interest to this study is a titanium alloy with 8% (by weight) aluminum and 1% erbium (Ti-8Al-1Er). For titanium alloys, aluminum is used as a solid-solution strengthener up to about 8 wt%. For aluminum content greater than 8 wt%, strength begins to suffer as an intermetallic is formed. The addition of erbium forms an oxide dispersion of nano-particles that also acts as a strengthener. However, erbium is not typically alloyed with titanium because the formation of the strengthening nano-dispersoids (Er_2O_3) requires some level of rapid solidification, which standard ingot production does not offer [4, 5]. Alloying titanium with erbium is well suited for EBF^3 processing as it involves high-cooling rates and rapid solidification. More commonly used titanium alloys were also considered for purposes of comparison, including Ti-6Al-4V, Ti-6Al-2Sn-4Zr-2Mo, commercially-pure (CP) titanium, and Ti-6Al-4V ELI (extra-low interstitial) which is a Ti-6Al-4V alloy having lower levels of impurities (e.g., oxygen and iron) than the standard alloy.

These titanium alloys were chosen for a number of reasons. First, they are chemically compatible in that there are no brittle intermetallic phases expected over the full range of possible mixtures and processing temperatures. Second, they have vastly different static mechanical properties. Finally, the mixtures are easy to quantify by measuring aluminum concentration (in solid solution) and also by measuring particle density of Er_2O_3 dispersoids in the case of Ti-8Al-1Er [4]. This will give an indication of the diffusion-based mixing effects (aluminum in solid solution) and convection-based mixing effects (Er_2O_3 in liquid titanium).

Samples of each material were produced for analysis and mechanical testing. Ultimately, the objective is to establish a link between processing, microstructure, and mechanical performance. Connecting these bodies of knowledge (processing, microstructure, and mechanical performance) with both experiment/observation and analysis/modeling is the ultimate objective of this effort. This approach is illustrated in Figure 2. Here, it is shown that processing history affects the resulting microstructure, which in turn affects the mechanical performance. Once this processing-to-performance relationship is understood for a given alloy, and incorporated into a predictive model, specific features that are detrimental to performance can be mitigated by altering processing parameters; this is illustrated in Figure 2 by the loop. Each pass through this "loop" is expected to refine the material performance, at least for a given performance attribute (e.g., strength, fatigue life).
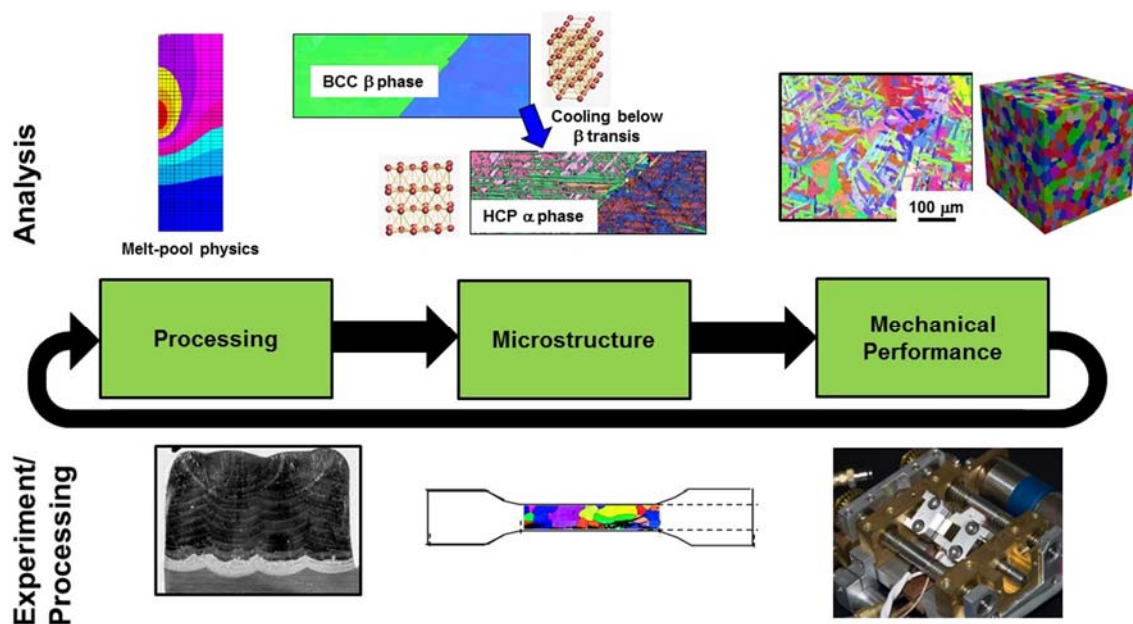
Figure 2. Schematic of iterative computationally-informed material design. Modeling of the EBF[3] process includes the melt-pool physics (illustrated schematically in the upper left), the distribution of solid phases upon cooling (upper center), which ultimately results in the final alloy microstructure (upper right). The resulting mechanical performance is characterized using in-situ testing (within a microscope; lower right). EBSD (electron back-scatter diffraction) is used to provide spatial characterization of microstructure (lower center). Optical microscopy (lower left) is also used to characterize microstructure at higher length scales.

3.   Materials Processing

Monolithic EBF[3] material was produced using titanium and titanium alloy wire feedstock deposited on grade 2 commercially-pure (CP) titanium plate substrates. Materials considered were Ti-8Al-1Er, CP-Ti, Ti-6Al-4V, Ti-6Al-2Sn-4Zr-2Mo, and Ti-6Al-4V ELI. Additionally, material was produced with compositional gradients or interfaces between CP-Ti and Ti-8Al-1Er. Here, the deposited material was created using grade 2 CP-Ti wire, Ti-8Al-1Er wire, or a combination of the two wires. Constant ratio mixtures were created using fixed feed rates for each of the two wires. A graded composition deposit was created by changing feedstock wire halfway through each layer (i.e., five rows of CP-Ti followed by five rows of Ti-8Al-1Er). As there is about 33% overlap between successive rows, there is some degree of mixing between the two alloys as the wire feedstock is changed. This creates a gradient in composition near the interface between the deposited materials. Mechanical testing was conducted on EBF[3] titanium monolithic and graded materials, including microhardness testing (Section 5.1), tensile testing (Section 5.2), fatigue crack growth testing (Section 5.3), and fatigue testing (Section 5.4). A photograph of a typical EBF[3] product is shown in Figure 3.
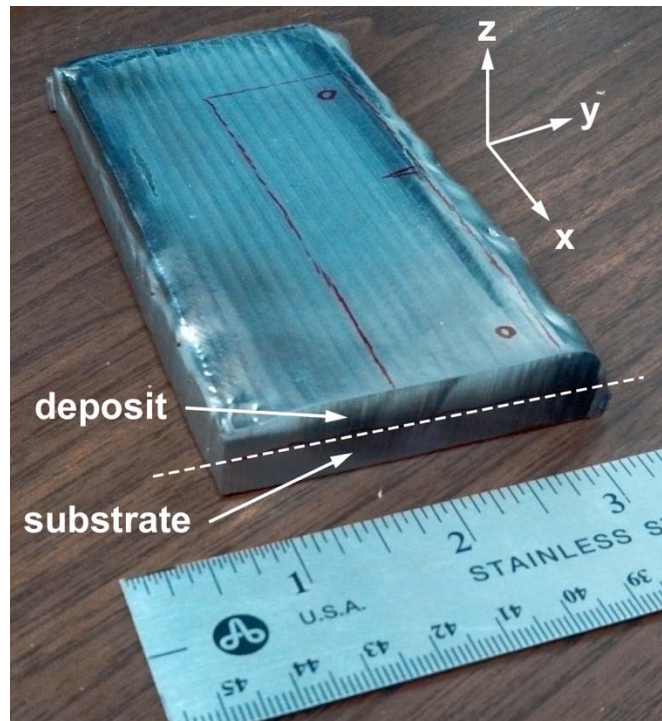
Figure 3. Photographs of typical EBF³ products used to produce fatigue crack growth specimens. Smaller specimens were used for microstructural characterization.

4.   Microstructural Characterization

Samples produced by EBF³ were analyzed to characterize the microstructure. This was done using both optical and scanning electron microscopy.

4.1. Optical microscopy

Samples of EBF³ were produced by depositing four side-by-side rows of material (each approximately 9 mm wide with an overlap of approximately 33%) to produce a product that was approximately 25 mm wide. Twelve layers were deposited, giving the samples a height of approximately 15 mm. The length of the samples was nominally 125 mm. The samples were sectioned normal to the deposit direction (x direction in Figure 3) and the cross sectional surface was then mounted in an epoxy metallurgical mount, polished, and lightly etched. Optical micrographs for each of the five alloys considered are shown in Figure 4. Here it can be seen that the Ti-8Al-1Er appears to have a scalloped appearance showing clearly each of the individual passes. This feature is unique among the alloys examined; with the exception of CP-Ti, the other three alloys have columnar grains, presumably a result of epitaxial grain growth from the multiple thermal cycles of individual deposition passes. CP-Ti appears to have a large grain structure without any obvious texture due to thermal processing. These observations suggest that the Ti-8Al-1Er alloy indeed is different from the other (more commonly used) titanium alloys. Unlike constituents in other titanium alloys, erbium acts as an oxygen getter,

6

producing erbia (Er_2O_3) precipitates in Ti-8Al-1Er, which strengthen the material by inhibiting dislocation motion [4]. Scanning electron microscopy was done on the Ti-8Al-1Er alloy to further investigate the microstructure.
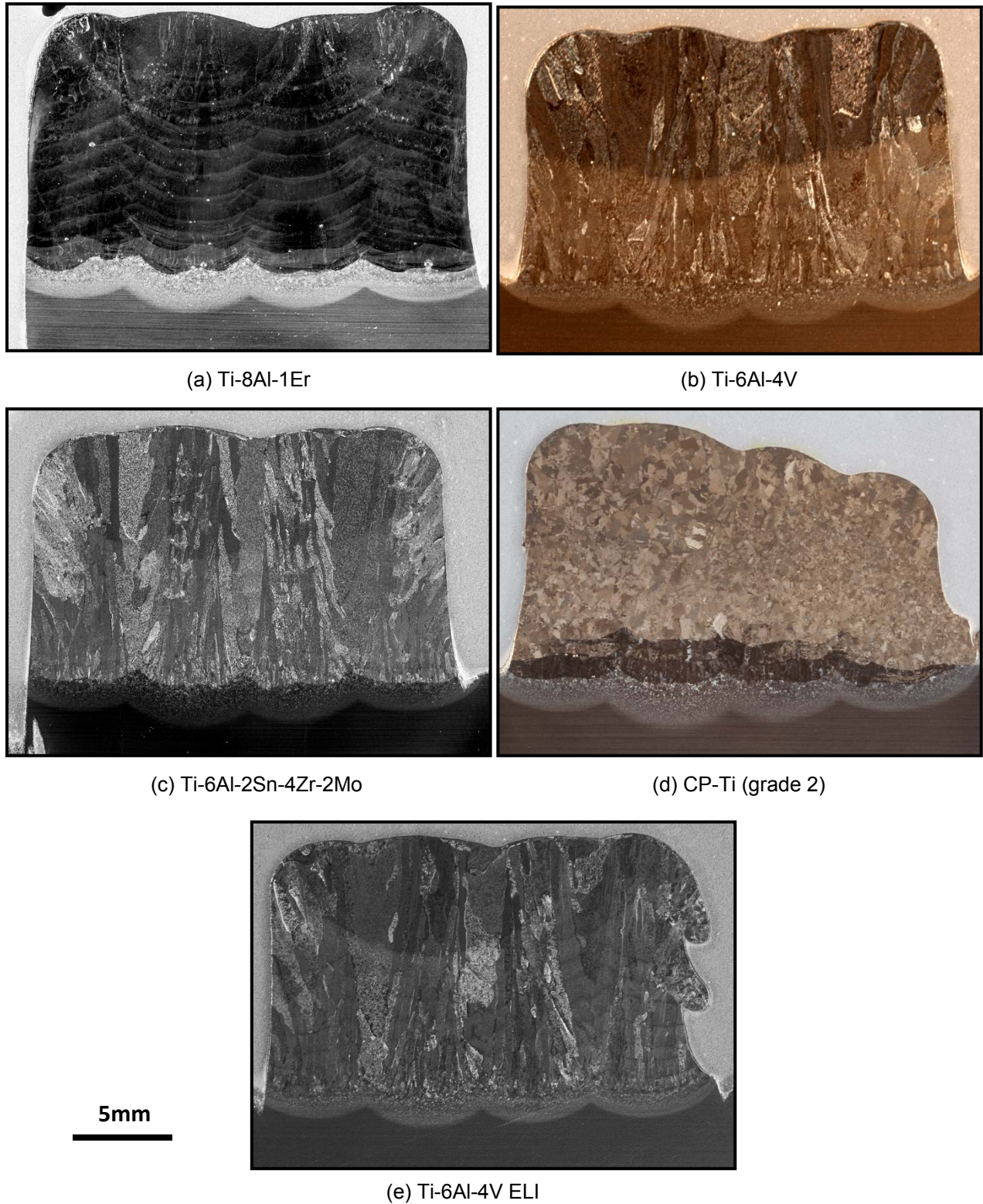

(a) Ti-8Al-1Er

(b) Ti-6Al-4V

(c) Ti-6Al-2Sn-4Zr-2Mo

(d) CP-Ti (grade 2)

(e) Ti-6Al-4V ELI

Figure 4. Optical microscopy images of EBF[3] products.

4.2. Scanning Electron Microscopy (SEM)

Tensile specimens were prepared from Ti-8Al-1Er material and polished for electron backscatter diffraction (EBSD) characterization. Specimens were loaded in the direction of wire deposition, also known as the "L" direction. The observed (polished) surface was normal to the plane of the substrate. The sample was mechanically polished, with the final polishing steps using a 1 micron and 3 micron diamond suspension. The final polishing step was colloidal silica mixed with reagent grade 30% hydrogen peroxide (H_2O_2). This polish resulted in an average band contrast (a dimensionless quality metric of EBSD patterns from Oxford Instruments' AZtecHKL software) of around 110, a value that suggests the patterns are readily indexable. EBSD characterization was performed using an Oxford Instruments AZtec EBSD system on a FEI/Phillips XL30 Environmental Scanning Electron Microscope (ESEM). Energy Dispersive Spectroscopy (EDS) analysis was performed on a HitachiS-3700N SEM equipped with an Oxford Instruments AZtec EDS system.

4.2.1. Electron Back-Scatter Diffraction (EBSD)

EBSD was employed to characterize the grain structure of the Ti-8Al-1Er. The average grain size of the material was about 16 microns, but the distribution was bimodal due to the high amount of twinning. A large number of compression twins were detected in the material before deformation. The characteristic misorientation angle of these twins was between 57 and 64 degrees, suggesting these twins were compression twins of the $\{1\ 0\ \bar{1}\ 1\}$ or $\{1\ 1\ \bar{2}\ 1\}$ type [6]. A smaller number of tensile twins with a characteristic plane of $\{1\ 0\ \bar{1}\ 2\}$ and a misorientation angle of 85 degrees were also detected. The twin fraction was so high, it is difficult to distinguish between parent and child grains to assess the twin fraction. In hexagonal materials, twin boundaries are often significant in crack initiation and propagation. For an example of this highly twinned microstructure, see Figure 5.

4.2.2. Energy Dispersive Spectroscopy (EDS)

Based on the processing parameters described above, we expected the majority of the erbia dispersoids in the material to be nanometer sized, too small to be properly resolved via SEM. Using backscatter imaging, a number of highly florescent particles around 0.25-1 micron in size were observed, which EDS confirmed were erbium rich. Because erbium is not miscible with hexagonal titanium at almost any concentration, we concluded that these large particles were simply unexpectedly large erbia (erbium oxide) particles, a hypothesis confirmed by the fact that these particles have EBSD patterns consistent with a cubic material (erbia is approximately cubic). These larger dispersoids are homogeneously distributed, see Figure 6. Closer inspection of the twin grain boundaries using a back scatter detector on a different region of the sample (see Figure 7) indicates that smaller nano-particles decorate the grain boundaries, including twin boundaries. The fact that the homogeneously distributed particles are larger than those on the grain boundaries suggests that nucleation of erbia particles is homogeneous and on subsequent passes erbia nucleates on the grain boundaries and pre-existing dispersoids grow. The effect of this distribution of erbia particles on fracture will be discussed in the next section.

Figure 5. An inverse pole figure (IPF) map of the highly twinned microstructure of the Ti-8Al-1Er alloy. The twins are compression twins with a misorientation of 57-64 degrees.
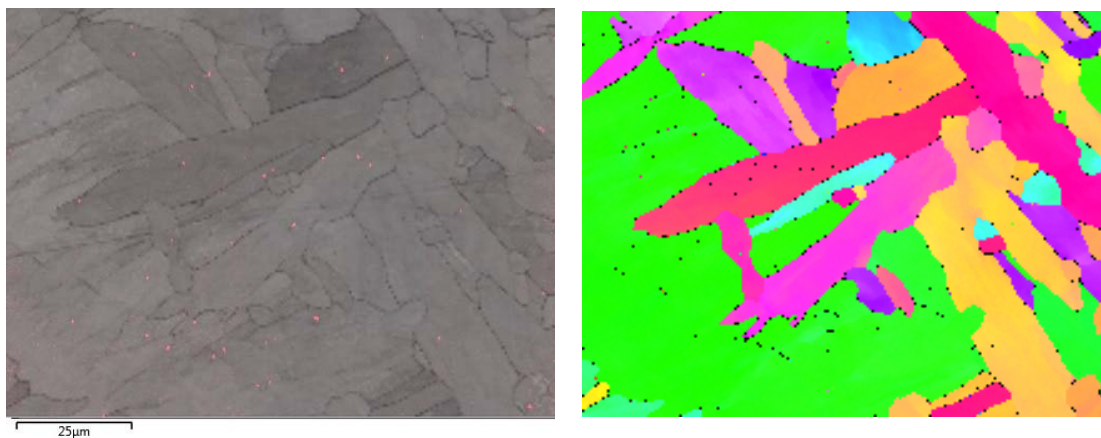

Figure 6. Band contrast image (left) with large erbium rich particles highlighted in pink and an inverse pole figure map (right) of a region of the Ti-8Al-1Er sample. Note that these larger florescent particles are homogeneously distributed, not along grain boundaries.

5.   Mechanical Testing and Results

Mechanical tests were run on the EBF[3] Ti-8Al-1Er and CP-Ti to characterize their performance. These tests include micro-hardness testing, tensile testing, fatigue crack growth, and fatigue testing.
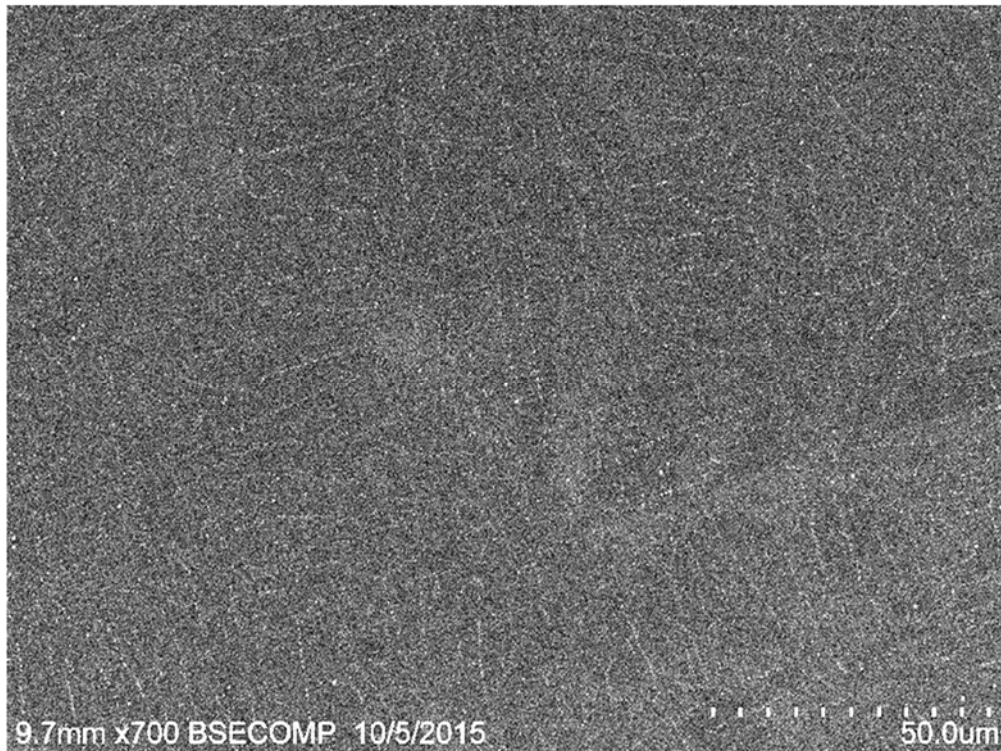
Figure 7. Back scatter image of fine erbia particles along grain and twin boundaries.

5.1. Micro-Hardness Testing Across a CP-Ti/TiAlEr Interface

A single layer deposited sample containing five rows of 100% CP-Ti with a step change to five rows of 100% Ti-8Al-1Er was used to evaluate the transition. A cross-section cut was made (the *y-z* plane in Figure 3) in this deposit and micro-hardness measurements (Vickers indenter with 300g force) were made at constant intervals across the entire deposit. The micro-hardness data are plotted in Figure 8. The hardness values in the CP-Ti deposit are approximately 140 VHN_{300gf}. A sudden increase in micro-hardness occurs at the interface, increasing from approximately 140 VHN_{300gf} to 240 VHN_{300gf} over a distance of about 1 mm. In the Ti-8Al-1Er deposit, the hardness increased slightly with distance from the interface (increasing from about 240 VHN_{300gf} to 290 VHN_{300gf} over a distance of about 8mm). This is attributable to the diminishing effects of dilution that occurs as successive rows are deposited further from the interface.
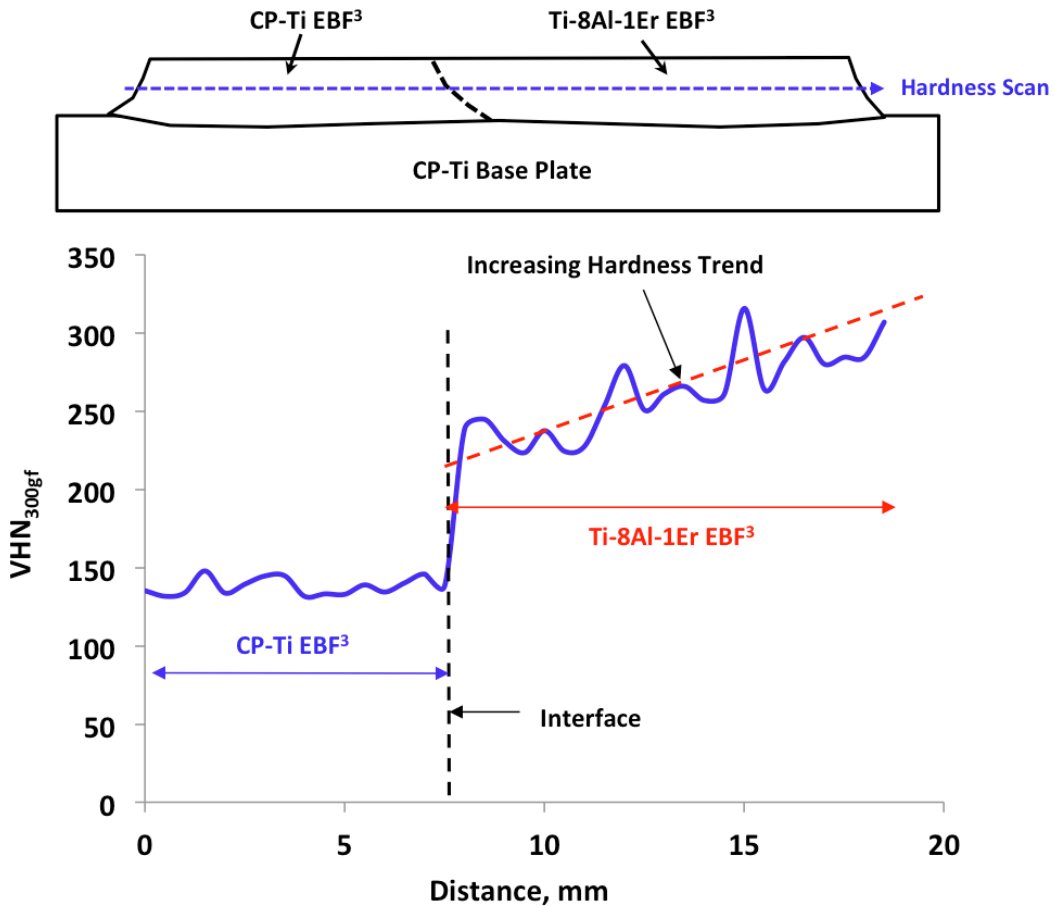
10

Figure 8. Micro-hardness test data across the interface of CP-Ti to Ti-8Al-1Er alloy of EBF³ deposited sample.

5.2. Tensile Testing

A total of 10 single-wall deposits were made for tensile testing (approximately 6 mm wide). Each deposited wall was approximately 250 mm long and 14 mm high. A 973 K, 2 hour vacuum anneal heat treatment was performed on all the deposited specimens prior to machining. From each wall, two flat dog-bone tensile test specimens were extracted using wire electro-discharge machining (EDM). The specimens had gage section dimensions of 32 mm long by 6.4 mm wide by 3.2 mm thick. Five different compositions were tested: 100% of each starting wire composition (Ti-8Al-1Er and CP-Ti) and mixed volumetric ratios of 25:75, 50:50, and 75:25. Four specimens were fabricated with each composition. Tensile testing was performed according to the ASTM Standard E8 [7].

The mechanical properties from tensile testing of the EBF³ products are shown in Figures 9 and 10 as a function of composition. The results shown in Figure 9 indicate a slight increase in elastic modulus (12%) as the composition varies from 100% CP-Ti to 100% Ti-8Al-1Er. This composition change also results in a reduction of elongation at failure (ductility) from approximately 50% to 10%. The data in Figure 10 indicate an increase in yield stress from approximately 240 MPa to 740 MPa due to the addition of the alloying elements (Al and Er). The strength increase can mainly be attributed to solid solution effects for aluminum and dispersoid effects for erbium. The trend is linear with respect to composition, implying a rule-of-

mixtures effect. The variation in ultimate tensile strength is similar in that it increases nearly linearly with increasing alloying elements, and increased from approximately 340 MPa (CP-Ti) to 810 MPa (Ti-8Al-1Er).
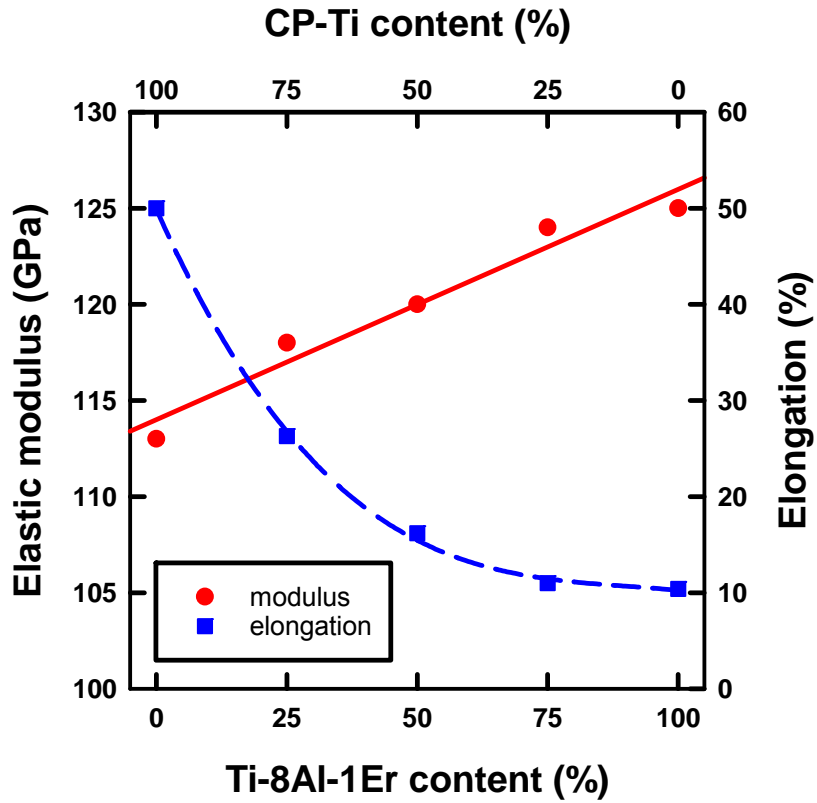

Figure 9. Tensile properties (elastic modulus and elongation) as a function of alloy content for EBF[3] deposited samples.
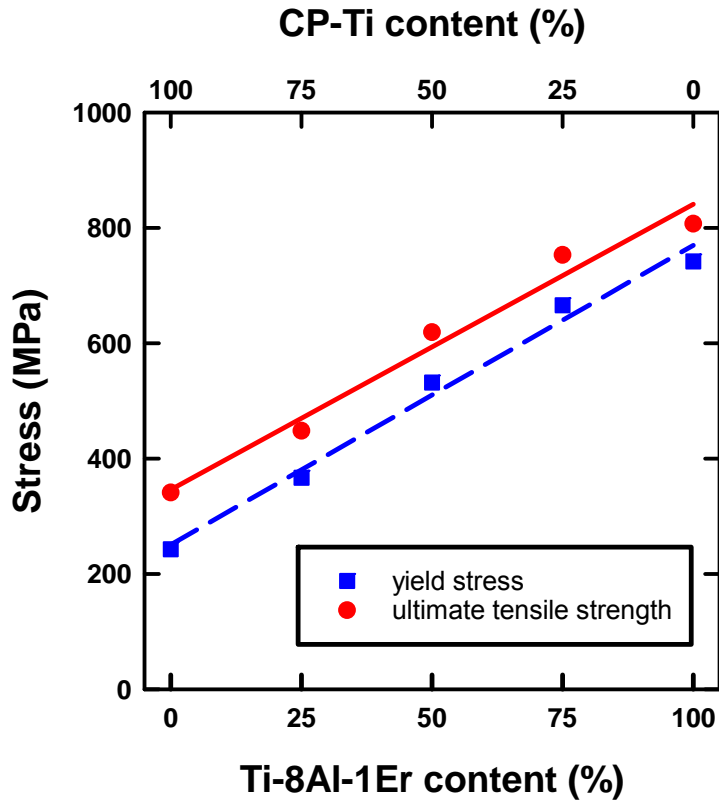
Figure 10. Tensile properties (ultimate and yield stress) as a function of alloy content for EBF^3 deposited samples.

5.3. Fatigue Crack Growth Testing

Deposited structures approximately 150 mm long by 63 mm wide were fabricated for fatigue crack growth testing. Within each structure, the deposited rows were approximately 6 mm wide and were oriented parallel to the loading axis of the crack growth specimens (the vertical direction in Figure 11(c)). A 973 K, 2 hour vacuum anneal heat treatment was performed on all samples prior to machining. Eccentrically-loaded single edge notch tension (ESE(T)) fatigue crack growth specimens were machined from the EBF^3 product forms. A schematic of the ESE(T) specimen configuration is shown in Figure 11(a) [8, 9]. The loading direction is parallel to the direction EBF^3 material was deposited and the crack is expected to grow across (perpendicular to) the EBF^3 deposited rows.
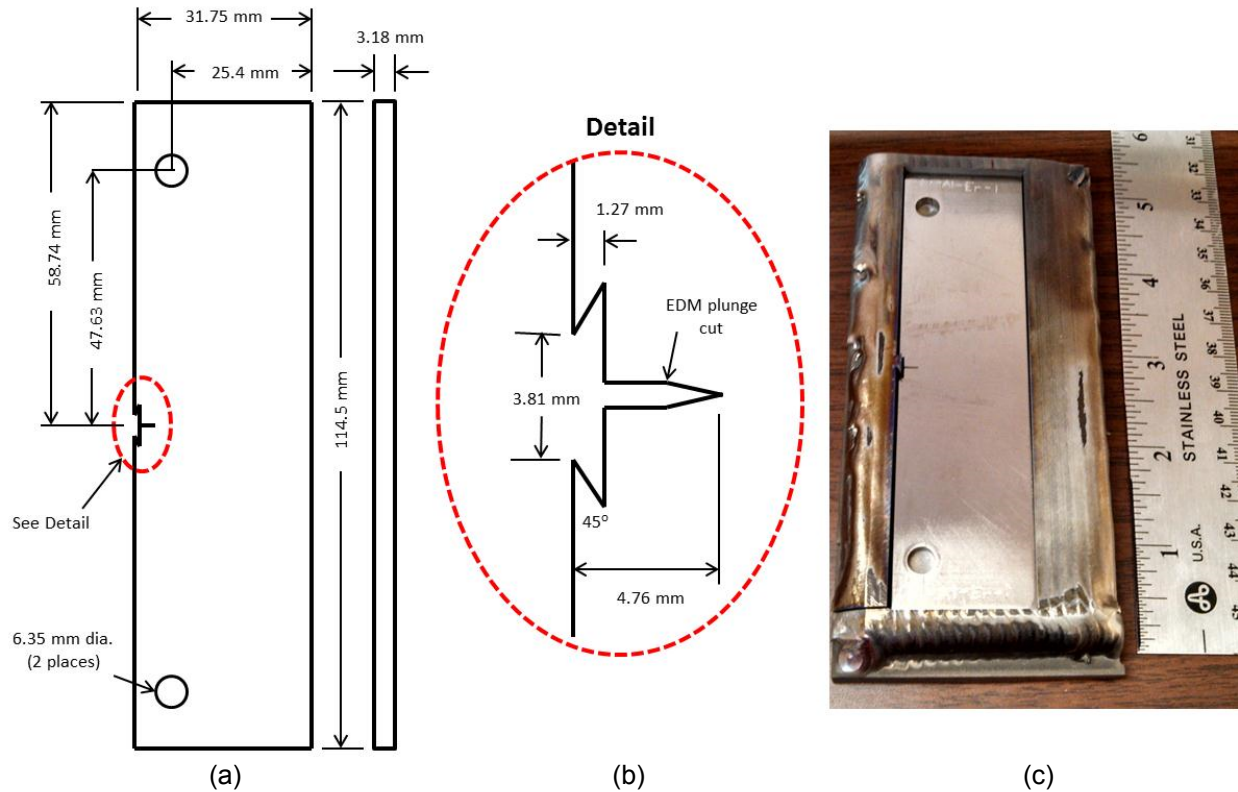
Figure 11. Fatigue crack growth specimen details: (a) ESE(T) specimen configuration, (b) detail of initial machined crack, and (c) specimen orientation with respect to EBF³ deposit.

Fatigue crack growth testing was performed in accordance with the ASTM Standard E647 [9]. During testing, crack length was monitored using a crack-mouth-opening displacement (CMOD) gauge and applied loads were continuously changed such that pre-determined values of the crack-tip stress intensity range (ΔK) were achieved [10]. Testing was conducted in room temperature laboratory air at a cyclic loading rate of 5 Hz and an R value of 0.1. Constant-ΔK testing was performed in this study to look for subtle changes in crack growth behavior as the crack propagated through the EBF³ deposited material [11, 12]. Maintaining constant ΔK is useful should the crack growth resistance vary as crack propagation occurs across boundaries between the EBF³ deposited rows.

Constant-ΔK test data is best plotted as crack length (*a*) versus cycle count (N). This data is presented in Figure 12 for a monolithic CP titanium specimen and a monolithic Ti-8Al-1Er specimen. The slope of these data is the fatigue crack growth rate (d*a*/dN). A fitted line through these data is used to determine the crack growth rate for ΔK = 7.9 MPa√m (with a load ratio, ratio of minimum to maximum load in a fatigue load cycle, of R = 0.1), for CP-Ti (blue triangular symbols) and for Ti-8Al-1Er (red square symbols). From these data, it can be seen that for a cyclic crack-tip stress intensity factor of ΔK = 7.9 MPa√m the CP-Ti material exhibits a crack growth rate approximately twice that of the Ti-8Al-1Er alloy (d*a*/dN = 3.55 x 10⁻⁹ m/cycle compared with d*a*/dN = 1.75 x 10⁻⁹ m/cycle, respectively). Further, the crack growth path did not exhibit any deviation that would have been expected if the boundaries between EBF³ deposition passes were relatively weak in fatigue crack growth resistance. This observation suggests that the material produced is rather homogenous in terms of fatigue crack growth

14

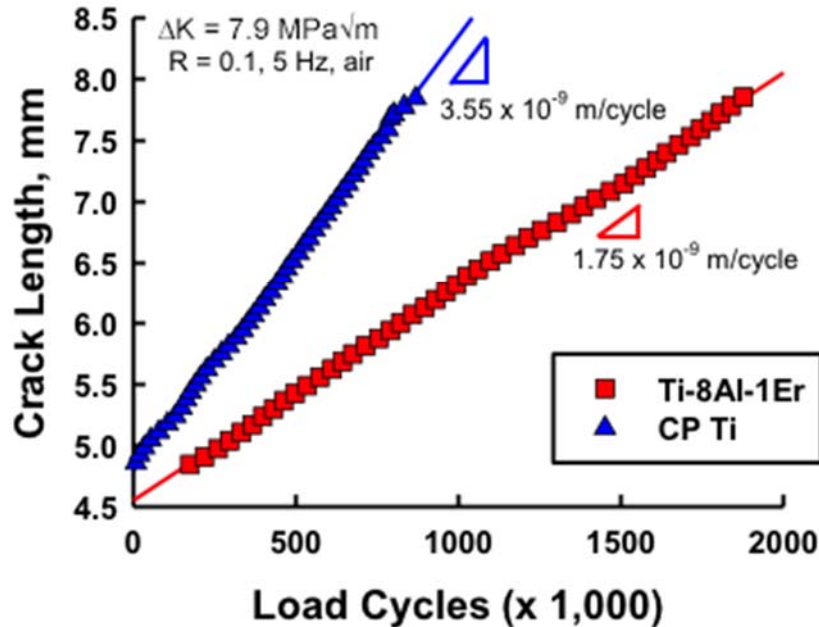performance. Also, the Ti-8Al-1Er material is more resistant to crack growth (lower crack growth rate).

Figure 12. Fatigue crack growth results from CP-Ti and Ti-8Al-1Er monolithic ESE(T) specimens fabricated by EBF[3]

The fatigue crack growth data for the composite specimen (described in Section 5.1) are plotted in Figure 13. This specimen was tested at a constant ΔK value of 9.9 MPa√m. Steady state crack growth data in the Ti-8Al-1Er material (da/dN = 4.15 x 10^{-7} m/cycle), indicated as red square symbols, was shown to occur between crack lengths of approximately 6 mm and 12 mm. Around a crack length of 12 mm, the crack began to propagate into the transition region between the two materials; these transient data are indicated as open circular symbols. Upon propagating into the CP-Ti region, steady state crack growth was re-established (blue triangular symbols; da/dN = 8.65 x 10^{-7} m/cycle) over a range in crack length between approximately 14 mm and 20 mm. Note that the earlier observation that the crack growth rates in CP-Ti were nearly a factor of 2 greater than for the Ti-8Al-1Er alloy (recall Figure 12; ΔK = 7.9 MPa√m) also is true at higher ΔK (= 9.9 MPa√m).

Photographs of the crack profiles are shown in Figure 14. Fatigue cracks can be seen originating at the crack starter notches on the left side of each photograph. The crack profile of the CP-Ti (Figure 14a) exhibited a few "jogs" where the crack briefly deviated from the direction perpendicular to the applied load. Two such jogs are shown in the red circle of Figure 14a. This seemed to occur along the boundaries between e-beam deposition rows, however, this did not produce any anomalous fatigue crack growth behavior. In comparison, the crack path of the Ti-8Al-1Er alloy, shown in Figure 14b, seems to be somewhat less tortuous and did not exhibit any jogs in the crack path for the specimen tested. A photograph of the crack path in a specimen with a gradient from Ti-8Al-1Er to CP-Ti is shown in Figure 14c; note that the Ti-8Al-

1Er region was better polished than the CP-Ti region despite being subjected to the same polishing procedure.   Presumably this is due to the differences in the mechanical properties (e.g., hardness) between the materials in the two regions.

The crack growth rate testing presented in this document was done at a load ratio of R = 0.1. At such low values of R, crack closure is expected to significantly affect fatigue crack growth rates, potentially more so for the relatively ductile CP-Ti [11, 12].
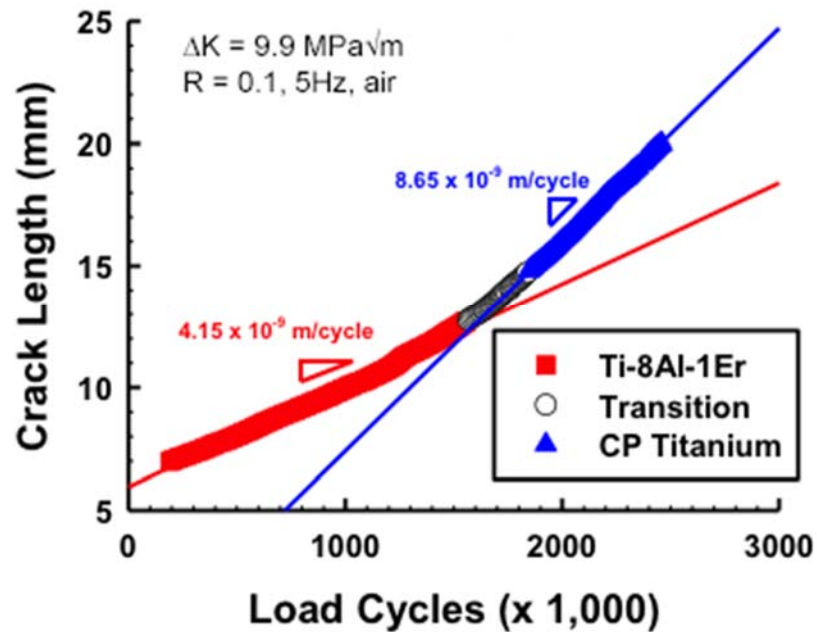

Figure 13. Fatigue crack growth results for gradient CP-Ti/Ti-8Al-1Er ESE(T) specimen fabricated by EBF[3].
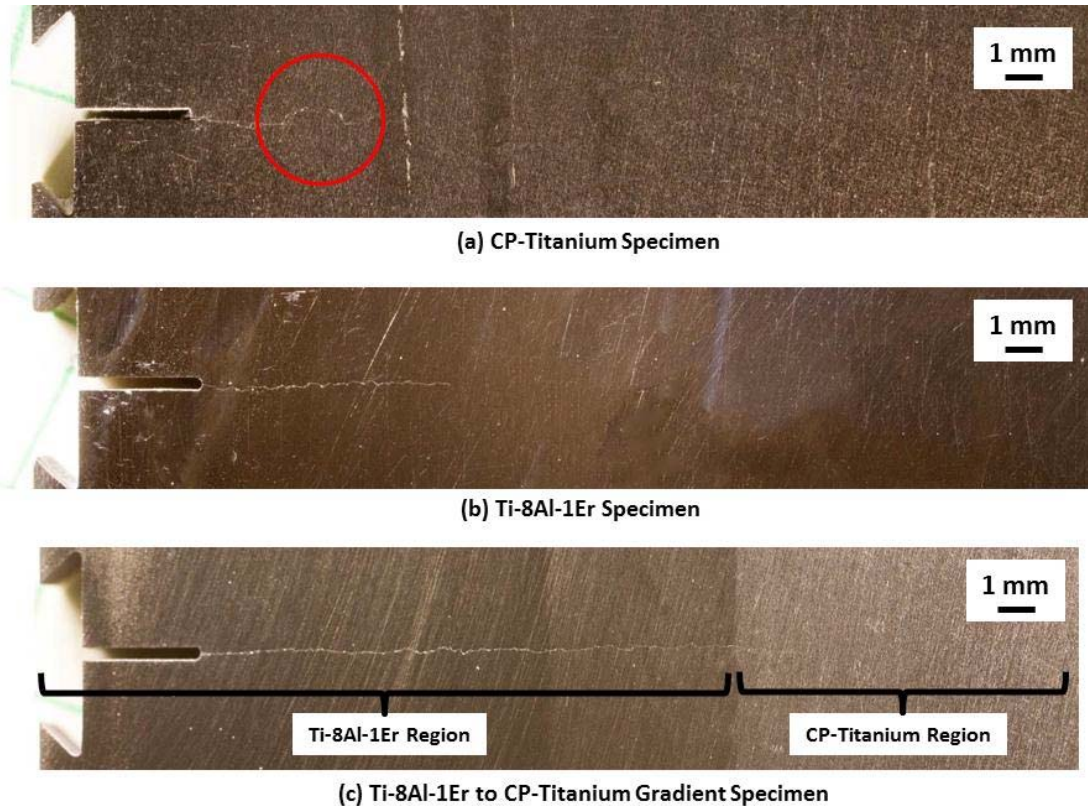
(a) CP-Titanium Specimen

(b) Ti-8Al-1Er Specimen

Ti-8Al-1Er Region   CP-Titanium Region

(c) Ti-8Al-1Er to CP-Titanium Gradient Specimen

Figure 14. Photographs of crack profiles for monolithic (a) and (b), and gradient (c) ESE(T) specimens fabricated by EBF[3].

5.4. Fatigue Testing

Fatigue testing was done using small dogbone tensile specimens shown schematically in Figure 15. Specimens were machined from monolithic (single titanium alloy) EBF[3] samples such that the loading direction (corresponding with the length of the specimen) aligned with the direction of wire deposit. Before testing, specimens were polished on one side to allow for EBSD characterization, then coated with a fine speckle pattern for digital image correlation strain-field analysis. The combination of EBSD (to characterize surface microstructure) and image correlation (to characterize surface strain field) potentially allows a direct correlation between microstructure and strain during mechanical testing. For this study, mechanical testing was performed on a servo-hydraulic test machine with optical microscopes (approximately 250X magnification) such that the strain-field resolution was on the order of the size of the grains within these alloys.

Testing was done using a servo-hydraulic test machine to apply sinusoidal loading with a peak load of P_{max} = 3.34 kN, a load ratio of R = 0.1, and a loading frequency of 5 Hz. The maximum value of stress was approximately σ_{max} = 518 MPa. During fatigue loading, digital images were captured at peak load once every 200 load cycles.
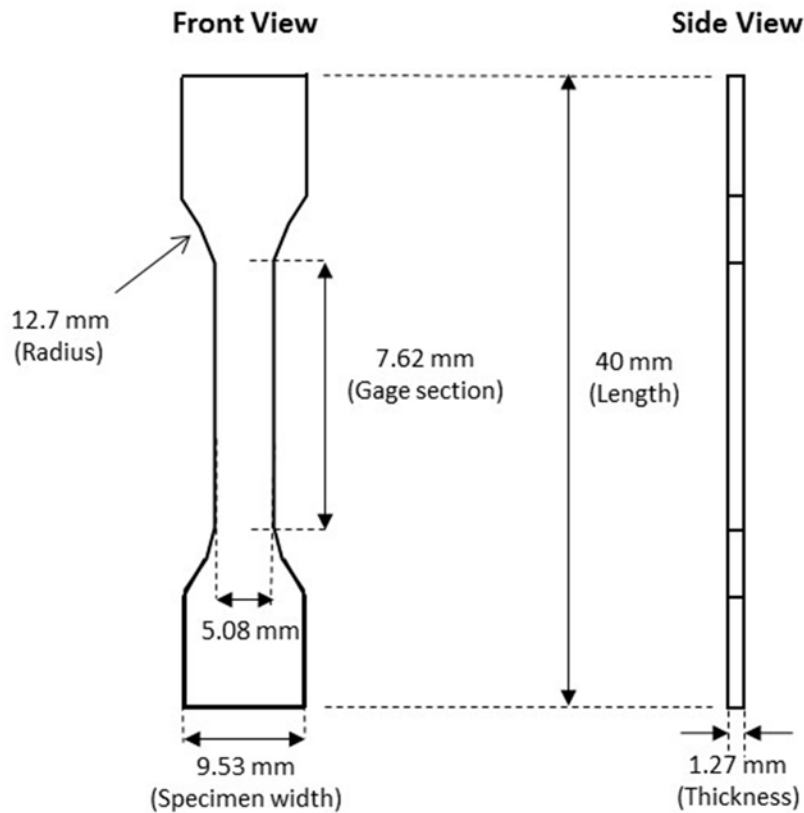
Figure 15. Schematic of small dogbone specimens used for fatigue testing.

5.4.2 – Crack Initiation and Microstructurally Small Propagation in Ti-8Al-1Er

The initiation site of the crack that eventually resulted in failure was not discovered. Instead, other crack nucleation events that did not proceed to failure were examined. There were fewer small cracks in the material than expected, and they all seemed to initiate from voids rather than from erbia particles. One nucleation site is shown in Figure 16. The crack appears to have been nucleated at the void. At the presumed nucleation site, two large debonded erbia particles can be seen. Their size and proximity constitute an extreme case of the microstructure, and it is possible they played some role in the crack nucleation event. Once nucleated, the crack propagated in a microstructurally small manner, following slip planes. The crack seems to ignore nearby erbia particles entirely, even when passing as close as a micron, suggesting that the erbia particles do not easily delaminate from the titanium matrix. Interestingly, this crystallographic behavior continues even in the presence of low energy twin boundaries, suggesting that the apparent grain refinement due to large amounts of compressive twinning during processing does not affect crack propagation.

In one examined region of the sample, a cluster of tensile twins was found, shown in Figure 17. The twins have a characteristic plane of $\{1\,0\,\bar{1}\,2\}$ and a misorientation angle of 85 degrees. Tensile twins in this material are generally thinner than the compression twins. These twins

18

were probably formed during processing, as there was no noticeable change in the twin fraction before and after deformation, and the sample was not significantly plastically deformed. As seen in the accompanying kernel average misorientation map, the region with a high tensile twin fraction is associated with strong localization of dislocation density. Twins may play an important role in deformation and fatigue, and may be readily controlled by controlling the texture of the material.
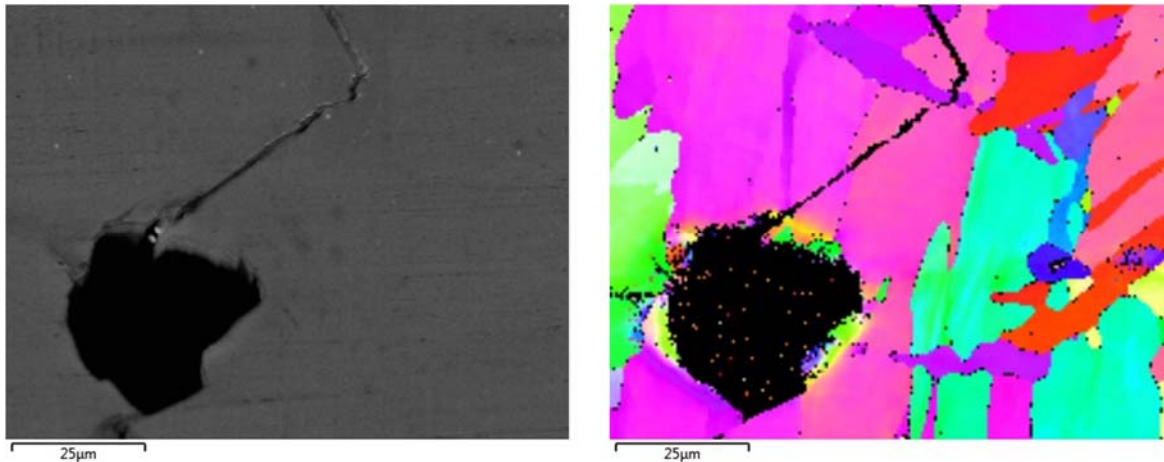

Figure 16. An electron image (left) and an IPF map of a region around a void where a crack nucleated. Note that the crack propagates along a straight, crystallographic direction and is not deflected by twin boundaries.

If processing parameters for this material were optimized and the void content reduced, other mechanisms may play a more important role in damage initiation. Therefore, while crack nucleation in this sample was affected by voids, localization due to other microstructural features was also examined. First, localization around an erbia particle was examined. Very high resolution EBSD diffraction patterns were collected in the region of an erbia particle, shown in Figure 17. The level of plastic deformation is approximated by using the kernel average misorientation, an analog of geometrically necessary dislocation density accumulation. While there is a noticeable increase in dislocation density around the particle compared to the surrounding matrix, it pales in comparison to a nearby slip band. The dislocation accumulation suggests that the particles play an important role in strengthening the material via the Orowan mechanism. So far, no evidence has been found that this dislocation accumulation culminates in fracture of the particle and/or delamination, as is typical of other hard particles.

In addition to the compression twins that are ubiquitous in the sample (due to processing), a much smaller amount of tensile twins were also found in one region of the sample, shown in Figure 18. The twins have a characteristic plane of $\{1\,0\,\bar{1}\,2\}$ and a misorientation angle of 85 degrees. Because an EBSD scan of sufficient resolution was not conducted of this region prior to failure, it is unclear whether these twins formed during processing, during fatigue loading, or during catastrophic failure. Their small size and the fact that multiple twins of the same orientation formed in the same grains suggest that they formed during load. As seen in the accompanying kernel average misorientation map, the highly twinned region is associated with strong localization of dislocation density. Twinning may play an important role in deformation and fatigue, and may be readily controlled by controlling the texture of the material.
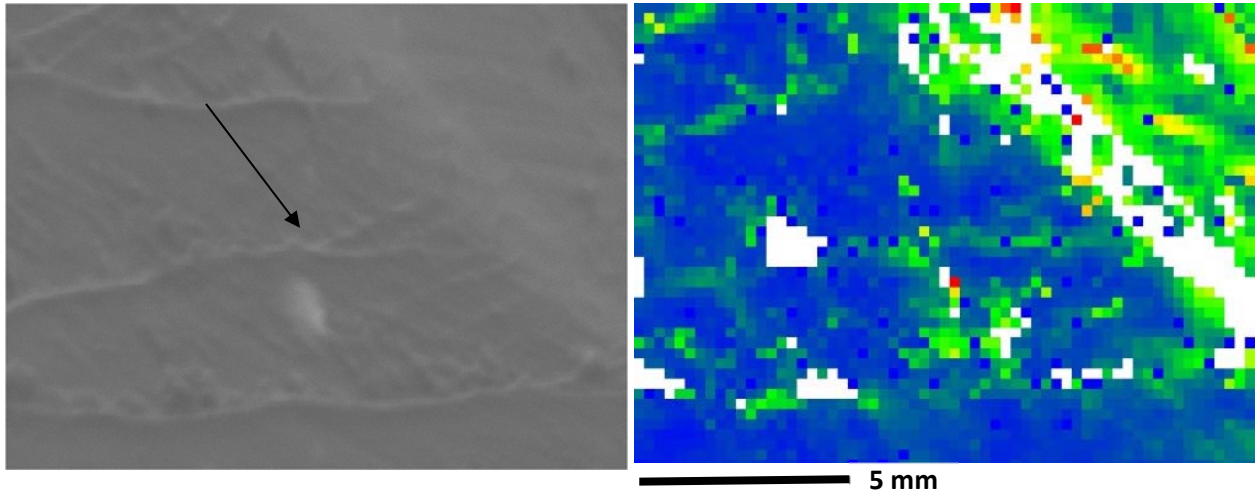
5 mm

Figure 17. Detail of an erbia particle (marked with an arrow) in a highly deformed region of the sample using both a secondary electron image (a) and a kernel average misorientation map (b).

5.4.2.2 Microstructurally Large Crack Propagation

In the previous section, no evidence was discovered of erbia particle involvement in fatigue crack propagation at small length scales. This remains true even at larger length scales. In Figure 19, an image of the fracture surface is shown where the crack is growing at a crack growth rate of approximately 1 micron per cycle. Here, the crack is through the thickness of the sample. While a number of erbia particles are visible in this region, none are delaminated and the crack front does not bow in their presence, suggesting no weakness and delamination.

Once the sample began to fail catastrophically, the fracture becomes more ductile, as seen in Figure 20. At this point, the erbia began to participate in the ductile failure of the material, and cup-and-cone structure is clearly visible with erbia particles visible in many "cups." Thus, while no evidence was found that the erbia dispersoids of this material negatively impact its fatigue life, they are probably responsible for the reduction in ductility under monotonic loading (recall Figure 9).
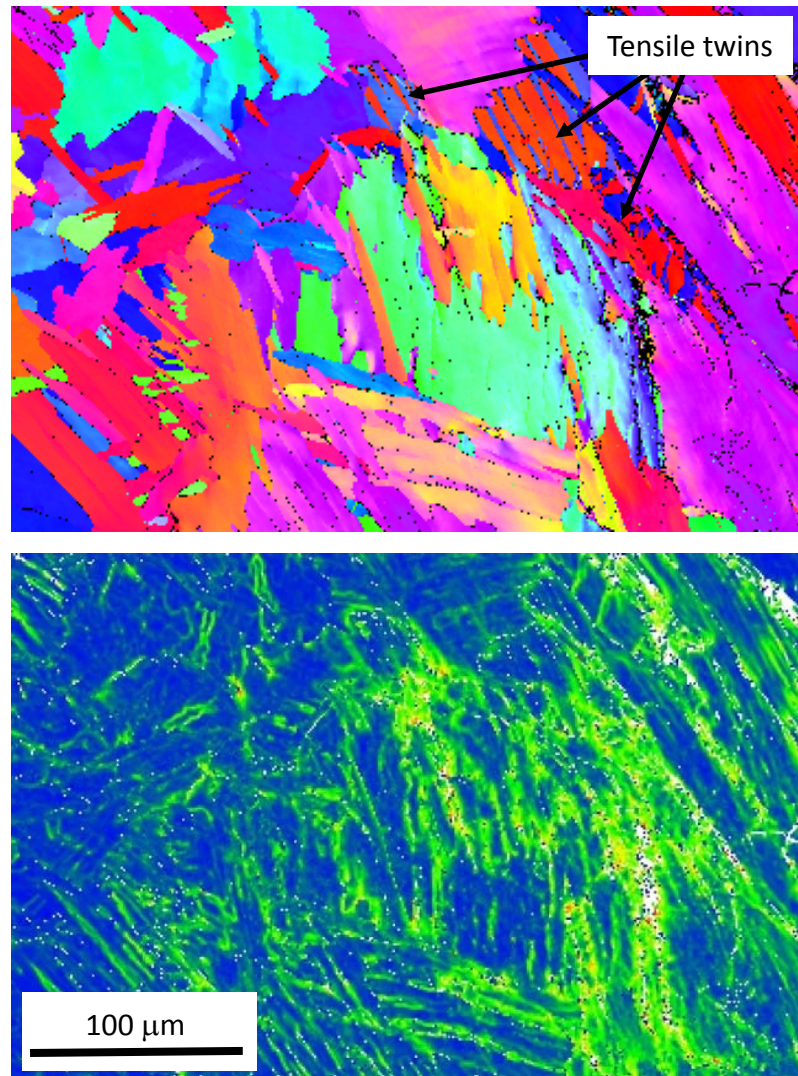
20

Figure 18. IPF map (above) and a kernel average misorientation map (below). Note the correlation of the tensile twins (marked) and regions of high kernel average misorientation.
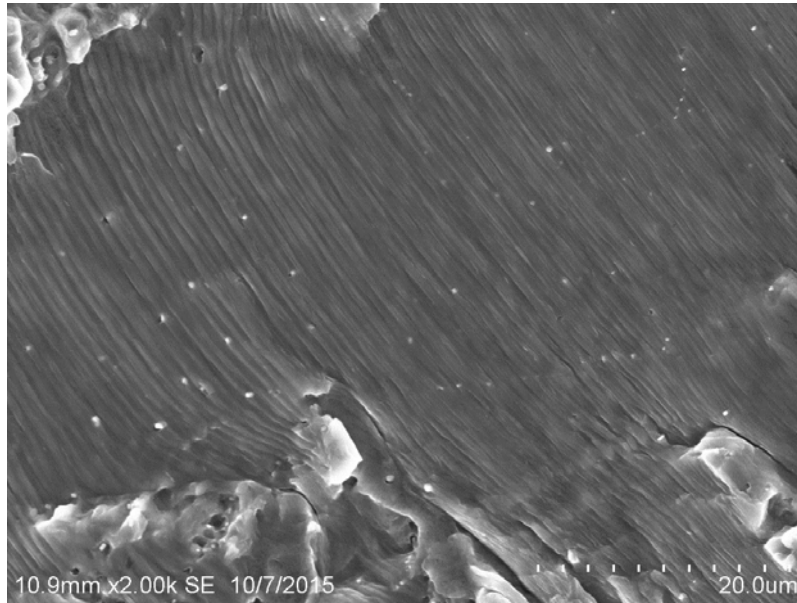
Figure 19. Electron image of the fracture surface where the crack was propagating under fatigue loading. Note that the crack front does not seem to be affected by the erbia particles.

Figure 20. Electron image of the fracture surface where ductile crack propagation rapidly occurred, leading to catastrophic failure. Note the cup-and-cone structure as it relates to the fluorescent erbia particles.

6.   Modeling of Materials

The complex crystallographic and morphological heterogeneities present in polycrystalline Ti-6Al-4V alloys result in localization of heterogeneous stresses and strains which govern where cracks can potentially nucleate within the bulk of the material. For instance, favorably oriented large grains [13] and a combination of hard and soft grains were observed to be preferred locations for crack initiation in Ti alloys subjected to fatigue [14]. Further, fatigue cracks in a Ti-

22

6Al-4V alloy (in both low-cycle fatigue and high-cycle fatigue regimes) formed mostly on basal slip planes and less frequently on prismatic slip planes [15]. Hence, microstructure plays a great role in crack initiation. It is worthwhile to understand how heterogeneous stress and strain localizes over the microstructural map of a material. Crystal plasticity finite element (CPFE) framework solves for the complex 3D stress and strain states and slip system activation within the microstructure, given a finite element representation of the microstructure of the material and the material response attributes (for instance, the orientation of grains, grain neighbors, elastic constants, hardening parameters etc.). For a detailed overview of the state-of-the-art CPFE models, refer to Raabe, et al. [16].

Over the past decade, several researchers have used the CPFE framework to understand the correlation between microstructural attributes and crack driving forces. Venkataramani et al. [17], using a dwell sensitive crystal plasticity model for Ti-6Al-2Sn-4Zr-6Mo, demonstrated that grains favorably oriented for basal slip transfer stress to nearby hard grains through load shedding. Dunne et al. [18] and Kirane et al. [14], using CPFE, demonstrated that certain types of "rogue" grain combinations (combinations of hard/soft grains) significantly increased crack driving forces. Anahid, et al., [19] used a well calibrated reduced order CPFE framework to calculate the dwell fatigue life of a Ti-6Al-2Sn-4Zr-6Mo alloy. Further, Przybyla, et al. [20] used extreme value correlations (sampled from simulating multiple number of statistical volume elements representative of microstructure of real material) to enable the identification and comparison of configurations of microstructural attributes that drive fatigue crack initiation (and hence result in the variability in fatigue life) in a duplex Ti-6Al-4V alloy. It is evident from aforementioned studies that fundamental insights regarding how microstructure affects the properties, and hence performance, of the material can be developed by using well calibrated and validated CPFE framework in conjunction with experimental data.

By leveraging a rate dependent CPFE framework, we aim to quantitatively understand the complex stress and strain heterogeneities within the microstructure of the material. A CPFE framework was used to solve for the heterogeneous stress state within the polycrystalline microstructure by combining anisotropic elasticity with rate-dependent crystal plasticity kinetics. For the purpose of this study, erbia particles haven't been explicitly considered within the microstructure, but they can be incorporated in the future studies. For the elastic behavior, individual grains within the microstructure were assigned five independent cubic elastic constants C_{11}, C_{12}, C_{13}, C_{33} and C_{44} equal to 153.97 GPa, 85.98 GPa, 67.16 GPa, 183.0 GPa, and 46.27 GPa, respectively [21]. Rate-dependent crystal plasticity kinetics (flow rule and hardening law) were assigned for the grains. The flow rule used for describing incremental slip on the slip systems is shown in Eq. 1:

$$\dot{\gamma}^\alpha = \dot{\gamma}_o \frac{\tau^\alpha}{g^\alpha} \left| \frac{\tau^\alpha}{g^\alpha} \right|^{\frac{1}{m}-1} \tag{1}$$

The slip resistance, g^α, shown in Eq. 2, evolves according to a gradient based evolution law obtained from combining the hardening laws given by Beaudoin et al. [22] and Voce-Kocks relations [23].

$$g^{\alpha} = H_0 \frac{\mu^2 b}{2(g^{\alpha} - g_0^{\alpha})} \sum_{k=1}^{N_{SS}} \sqrt{(\hat{n}_p^k : \Delta^T)(\Delta : \hat{n}_p^k)} \left|\dot{\gamma}^k\right| + G_0 \left(\frac{g_s^{\alpha} - g^{\alpha}}{g_s^{\alpha} - g_0^{\alpha}}\right) \sum_{k=1}^{N_{SS}} \left|\dot{\gamma}^k\right| , \qquad (2)$$

where g_0^{α} and g_s^{α} are the initial and saturation resolved shear strengths of slip system α; N_{SS} represents the number of slip systems; H_0 and G_0 are the direct hardening coefficients; b is the Burgers vector; $\hat{n}_p$ is the slip plane normal; and Δ is the measure of dislocation density and is calculated using the gradient of plastic deformation as shown in Eq. 3,

$$\Delta_{ij} = \epsilon_{jkl} F_{il,k}^p . \qquad (3)$$

In addition to the elastic constants, there are 7 calibrated parameters ($\dot{\gamma}_0$, m, H_0, G_0, g_0^{α}, g_s^{α} and μ) in the crystal plasticity model used in the current framework. The parameters were iteratively tuned in order to fit the macroscopic stress strain curve obtained from simulations to that obtained from tensile tests done at room temperature. The final calibration parameters of the crystal plasticity framework are shown in Table 1.

Table 1. Calibrated parameters to fit the macroscopic stress strain curve of Ti-64 at room temperature.

Parameter	Value
$\dot{\gamma}_0$ (s^{-1})	0.001
m	0.048
H_0 (MPa)	400.0
G_0 (MPa)	400.0
g_0^{α} (MPa)	257.3
g_s^{α} (MPa)	280.2
μ (GPa)	46.27

For the purpose of quantitatively understanding the heterogeneous stress state within the microstructure, a CPFE simulation was run on a digitally reconstructed microstructural region obtained from a well-polished test specimen. First, a 3D model of the microstructure was created by extruding the EBSD scan in the Z direction, using DREAM.3D [24]. Second, the surface meshes of grains created using DREAM.3D were exported to Gmesh [25] to generate a 3D volume mesh of the microstructure model. The final volume mesh (of the microstructure shown in Figure 21) was composed of 5,236,217 quadratic tetrahedral elements and 8,286,565 nodes. An in-house finite element package, ScIFEi [26], was used to carry out the CPFE simulation. A macroscopic strain of 1% was applied to the microstructure, and the simulation took approximately 3.5 hours to complete, when run in parallel on 256 processers.

Table 2. Model boundary conditions.

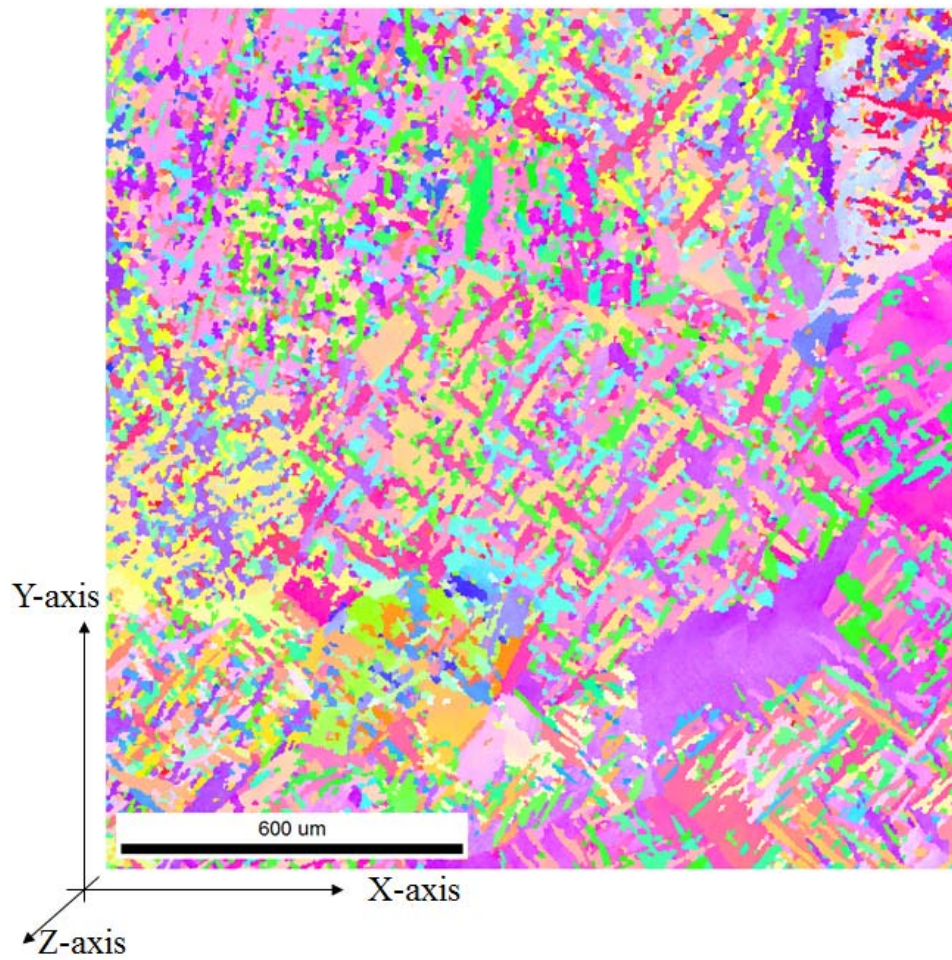| Boundary face	Boundary condition
-X	Fix X displacement
+X	Apply X displacement
-Y	Fix Y displacement
+Y	Free
-Z	Fix Z displacement
+Z	Free

Figure 21. EBSD scan taken on a polished surface of a Ti-8Al-1Er test specimen.
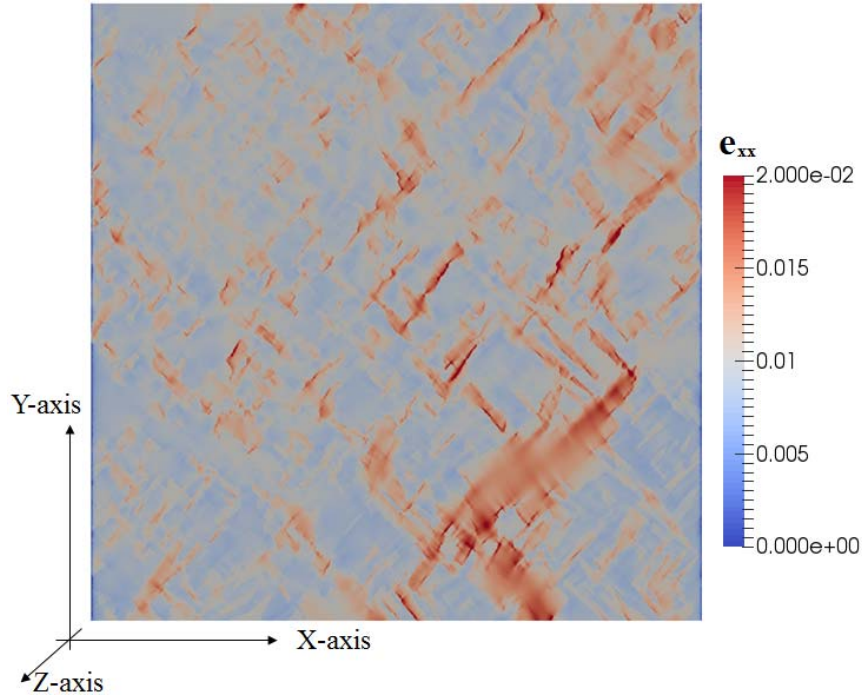
Figure 22. Strain component (e_{xx}) in the loading direction (XX) calculated from CPFE simulation using the microstructure shown in Figure 21. The strain map was obtained at an applied macroscopic strain of 1%.
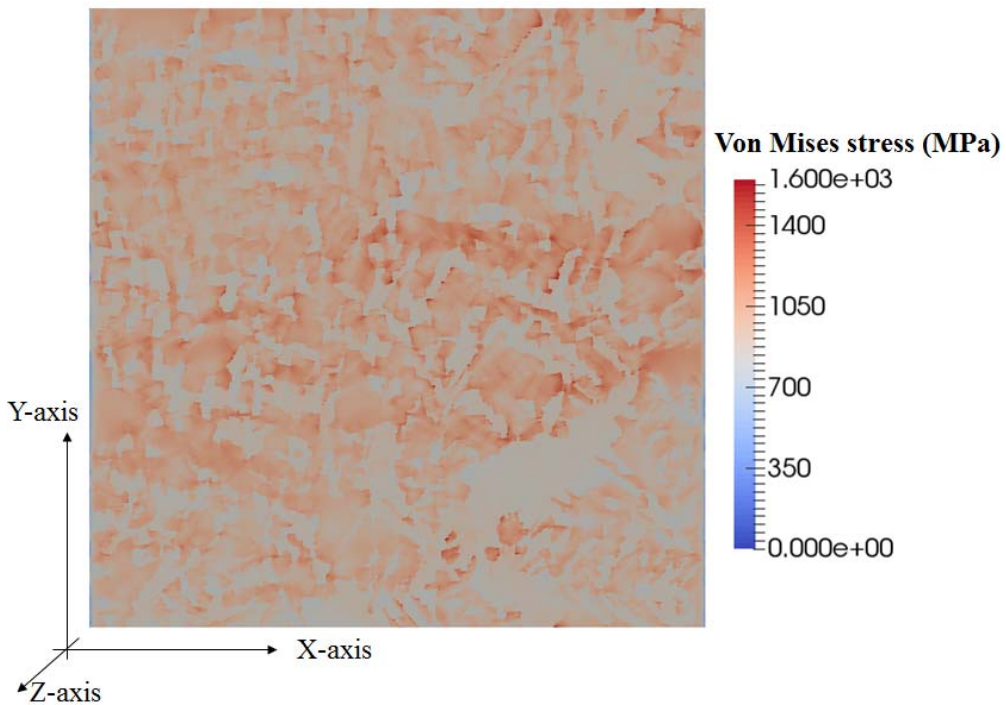

Figure 23. The von Mises stress calculated from CPFE simulation using the microstructure shown in Figure 21. The results show high stress concentrations within some favorably oriented grains. The stress map was obtained at an applied macroscopic strain of 1%.

Figure 22 shows the strain component in the loading direction. It can be seen from the strain map that some of the favorably oriented grains (aligned approximately 45 degrees to loading direction, XX) show high strain localization. Figure 23 shows the von Mises stress map on the microstructure. Specific locations within the microstructure are subjected to stress almost twice that of the average cross-sectional stress of 800 MPa. These high stress regions could be the hot-spots where cracks could initiate. Characterization of these hot-spots from the microstructural point of view will help establish a link between the microstructural attributes (like orientation/activation of basal or prismatic slip, combination of hard and soft grains, etc.) and crack driving forces (determined using the fatigue indicator parameters). This will be the focus of future studies.

7.   Discussion/Next Steps

As with other additive manufacturing methods, EBF[3] allows components to be "built-up" instead of "machined down," which significantly reduces wasteful machining byproducts (e.g., chips from traditional machining processes). Further, by changing the wire product or processing parameters, EBF[3] allows for development of materials with gradients in composition, microstructure, and mechanical properties. While creating such gradients is not a new idea, further work is needed to develop a physics-based understanding of the interrelations of (1) the composition and processing parameters with the resulting microstructure and (2) the microstructure with the resulting mechanical performance. The work presented in this document is a first step towards establishing this knowledge. Ultimately, such efforts will permit the design of advanced materials with specific mechanical performance (e.g., crack growth resistance) based on alloy composition and processing parameters. This would reduce the dependence on empirical experimental results, which would decrease the time and costs associated with certification of new materials for use in aerospace structures.

The next steps towards continuation of this work include: (1) developing process modeling capability and (2) modeling the material response at smaller length scales. As indicated in Figure 2, the ultimate goal is to relate processing parameters to microstructure and mechanical performance. Doing so requires process modeling capability which has not been explored in the current effort. The analysis results shown in Section 6 were done using crystal plasticity, which is a continuum-mechanics-based modeling method typically capturing microstructural features on the order of grain dimensions (nominally hundreds of microns). Capturing the influence of the erbia dispersoids (typically tens of nanometers in diameter) requires analysis to be done at a much smaller length scale. Future efforts would require the use of advanced analysis tools that include dislocation dynamics or molecular dynamics.

8.   Summary

Electron beam freeform fabrication (EBF[3]) Ti products were produced to show the feasibility of fabricating metallic materials with gradients in composition and mechanical properties. Materials were made with a gradient between CP-Ti and Ti-8Al-1Er. Experimental data presented in this document show that chemical gradients can be created in EBF[3] deposited

material that result in mechanical gradients in yield stress, ultimate tensile stress, elastic modulus, elongation at failure (ductility), hardness, and fatigue crack growth rates.

Tensile tests on monolithic samples showed that the Ti-8Al-1Er material had a yield strength of 740 MPa, a modulus around 12 % greater than CP Ti, and about half the elongation. Tests on monolithic blends of Ti-8Al-1Er and CP Ti showed that these properties followed the rule of mixtures. The fatigue crack growth rate of Ti-8Al-1Er was about half that of CP Ti. Finally, microhardness tests and a fatigue crack growth test on a composite sample showed that diffusion results in a smooth transition of properties at the interface of the two materials.

Microscopy results suggest that the erbia particles in the Ti-8Al-1Er material have a bimodal size distribution, with larger particles being homogeneously distributed, and smaller particles nucleating at the grain boundaries. Dislocation build up around these particles suggests that they contribute to the strength of the material, while at the same time post mortem analysis suggests that these particles do little to contribute to fatigue crack growth. However, the larger particles do contribute to the ductile failure of the material, as shown in the ductile fracture surface.

There remains a good deal of experimental testing that should be conducted on the 1-D material produced for this study. To ensure that the fatigue crack growth trends observed in Figure 8 hold in the absence of crack closure, additional fatigue crack growth testing of gradient materials should be done at a higher value of R where crack closure is expected to have a negligible role (e.g., R = 0.5).

The EBF[3] method deposits material in rows of a finite width; in this study, the rows were approximately 6 mm wide. It is possible that periodic variations in some material properties may occur with respect to the direction normal to the plane of deposition. Although tensile testing has been done on these materials, it was done using extensometers that might fail to capture such periodic variation in strain fields. Therefore, additional testing is planned to perform tensile testing using digital image correlation method, which will provide full-field strain data rather than a single scalar value from an extensometer.

Finally, in order to use a computational approach for science-based design of structurally graded materials, an analytical model will be generated of the mechanical test response of these materials. Although the materials produced for this study had a gradient in only one direction (1-D), ultimately, the models will be generated for materials with gradients in multiple directions (2-D and fully 3-D gradients).

9.   References

[1] ASTM International, "Standard Guide for Evaluating Mechanical Properties of Metal Materials Made via Additive Manufacturing Processes," ASTM F3122, ASTM International, West Conshohocken, PA (2014).

[2] K.M.B. Taminger and R.A. Hafley, "Electron Beam Freeform Fabrication: A Rapid Metal Deposition Process,' *Proceedings of the 3rd Annual Composites Conference*, Troy, Michigan (2003).

[3] J.Y. Hascoet, P. Muller, and P. Mognol, "Manufacturing of Complex Parts with Continuous Functionally Graded Materials (FGM),' *Proceedings of the Solid Freeform Fabrication Symposium.* Austin, Texas, USA (2011).

[4] C.A. Brice and H.L. Fraser, "Characterization of Ti-Al-Er Alloy Produced via Direct Laser Deposition," *Journal of Materials Science*, Vol. 38 (2003), pp. 1517-1521.

[5] C.A. Brice, J.A. Newman, R.K. Bird, R.N. Shenoy, J.M. Baughman, and V.K. Gupta, "Electron Beam Freeform Fabrication of Titanium Alloy Gradient Structures," NASA/TM-2014-218508 (2014).

[6] N. Stanford, U. Carlson, and M.R. Barnett, "Deformation Twinning and the Hall-Petch Relation in Commercial Purity Ti," *Metallurgical and Materials Transactions A*, Vol. 39A (2008) pp. 934-944.

[7] ASTM International, "Standard Test Method for Tension Testing of Metallic Materials," ASTM E8, ASTM International, West Conshohocken, PA (2014).

[8] R.S. Piascik, J.C. Newman, Jr., and J.H. Underwood, "The Extended Compact Tension Specimen," *Fatigue and Fracture of Engineering Materials and Structures*, Vol. 20 (1997) pp. 559-563.

[9] ASTM International, "Standard Test Method for Measurement of Fatigue Crack Growth Rates," ASTM E647, ASTM International, West Conshohocken, PA (2011).

[10] A. Saxena and S.J. Hudak, Jr., "Review and Extension of Compliance Information for Common Crack Growth Specimens," *International Journal of Fracture*, Vol. 14 (1978) pp. 453-468.

[11] W.T. Riddell and R.S. Piascik, "Stress Ratio Effects on Crack Opening Loads and Crack Growth Rates in Aluminum Alloy 2024," *ASTM STP 1332*, T.L. Panontin and S.D. Sheppard, Eds., American Society for Testing and Materials, West Conshohocken, Pennsylvania (1999).

[12] J.A. Newman, "The Effects of Load Ratio on Threshold Fatigue Crack Growth in Aluminum Alloys," Ph.D. dissertation, Virginia Polytechnic Institute and State University, Blacksburg, Virginia (2000).

[13] C. J. Szczepanski, S. K. Jha, J. M. Larsen, and J. W. Jones, "Microstructural Influences on Very-high-cycle Fatigue-crack Initiation in Ti-6246," *Metallurgical and Materials Transactions A*, Vol. 39A (2008) pp. 2841–2851.

[14] K. Kirane and S. Ghosh, "A Cold Dwell Fatigue Crack Nucleation Criterion for Polycrystalline Ti-6242 using Grain-level Crystal Plasticity FE Model," *International Journal of Fatigue*, Vol. 30 (2008) 2127–2139.

[15] F. Bridier, P. Villechaise, and J. Mendez, "Slip and Fatigue Crack Formation Processes in an α/β Titanium Alloy in Relation to Crystallographic Texture on Different Scales," *Acta Materialia*, Vol. 56 (2008) pp. 3951–3962.

[16] F. P. Eisenlohr, L. Hantcherli, D.D. Tjahjanto, T.R. Bieler, and D. Raab, "Overview of Constitutive Laws, Kinematics, Homogenization and Multiscale Methods in Crystal Plasticity Finite-element Modeling: Theory, Experiments, Applications," *Acta Materialia*, Vol. 58 (2010) pp. 1152-1211.

[17] G. Venkataramani, D. Deka, and S. Ghosh, "Crystal Plasticity Based FE Model for Understanding Microstructural Effects on Creep and Dwell Fatigue in Ti-6242," *Journal of Engineering Materials and Technology, Transactions of the ASME*, Vol. 128 (2006) pp. 356–365.

[18] F.P.E. Dunne, D. Rugg, and A. Walker, "Length-scale-dependent, Elastically Anisotropic, Physically-based HCP Crystal Plasticity: Application to Cold-dwell Fatigue in Ti Alloys," *International Journal of Plasticity*, Vol. 23 (2007) pp. 1061–1083.

[19] M. Anahid, M.K. Samal, and S. Ghosh, "Dwell Fatigue Crack Nucleation Model Based on Crystal Plasticity Finite Element Simulations of Polycrystalline Titanium Alloys," *Journal of the Mechanics and Physics of Solids*, Vol. 59 (2011) pp. 2157–2176.

[20] C.P. Przybyla and D. L. McDowell, "Simulation-based Extreme Value Marked Correlations in Fatigue of Advanced Engineering Alloys," *Procedia Engineering 2* (2010) pp. 1045–1056.

[21] R. Boyer and G. Welsch, Materials Properties Handbook: Titanium Alloys, 1994.

[22] A.J. Beaudoin, A. Acharya, S.R. Chen, D.A. Korzekwa, and M.G. Stout, "Consideration of Grain-size Effects and Kinetics in the Plastic Deformation of Metal Polycrystals," *Acta Materialia*, Vol. 48 (2000) pp. 3409-3423.

[23] F. Kocks, "Laws for Work-hardening and Low-temperature Creep," *Journal of Engineering Materials Technology*, Vol. 98 (1976) pp. 76-85.

[24] M. Groeber and M. Jackson, "DREAM3D: A Digital Representation of the Environment for the Analysis of Microstructure in 3D," *Integrating Materials and Manufacturing Innovation*, Vol. 3:5 (2014).

[25] C. Geuzaine and J.F. Remacle, "Gmsh: A Three-dimensional Finite Element Mesh Generator with Built-in Pre- and Post-processing Facilities," http://gmsh.info/

[26] J.E. Warner, G.F. Bomarito, G. Herber, and J.D. Hochhalter, "Scalable Implementation of Finite Elements by NASA_Implicit (ScIFEi)," NASA/TM-2016-219180.

REPORT DOCUMENTATION PAGE

1. REPORT DATE *(DD-MM-YYYY)*	2. REPORT TYPE	3. DATES COVERED *(From - To)*
1-11-2018	Technical Memorandum	

4. TITLE AND SUBTITLE

Characterization of Titanium Alloys Produced by Electron Beam Directed Energy Deposition

5a. CONTRACT NUMBER

5b. GRANT NUMBER

5c. PROGRAM ELEMENT NUMBER

6. AUTHOR(S)

Newman, John A.; Tayon, Wesley A.; Ruggles, Timothy J.; Brice, Craig A.; Yeratapally, Saikumar R.; Hochhalter, Jacob D.; Baughman, James M.; Claytor, Harold D.

5d. PROJECT NUMBER

5e. TASK NUMBER

5f. WORK UNIT NUMBER

869021.05.07.02.99

7. PERFORMING ORGANIZATION NAME(S) AND ADDRESS(ES)

NASA Langley Research Center
Hampton, VA 23681-2199

8. PERFORMING ORGANIZATION REPORT NUMBER

L-20975

9. SPONSORING/MONITORING AGENCY NAME(S) AND ADDRESS(ES)

National Aeronautics and Space Administration
Washington, DC 20546-0001

10. SPONSOR/MONITOR'S ACRONYM(S)

NASA

11. SPONSOR/MONITOR'S REPORT NUMBER(S)

NASA-TM-2018-220111

12. DISTRIBUTION/AVAILABILITY STATEMENT

Unclassified-
Subject Category 26
Availability: NASA STI Program (757) 864-9658

13. SUPPLEMENTARY NOTES

14. ABSTRACT
Functionally graded materials offer the potential to improve structural efficiency by allowing the material composition and/or microstructural features to spatially vary within a component. Additive manufacturing techniques enable the fabrication of such graded materials and structures. While examining several titanium alloys, this paper focuses on Ti-8Al-1Er as it has a unique microstructure that is only feasible when produced by rapid solidification methods like electron beam directed energy deposition, an additive manufacturing process. The results show that, when mixed, Ti-8Al-1Er and commercially-pure titanium uniformly mix at various ratios and the resultant static tensile properties of the mixed alloys behave according to rule-of-mixtures. At discontinuous interfaces between Ti-8Al-1Er and commercially-pure titanium, the crack growth behavior progresses smoothly across the discontinuity as the crack transitions from one crack growth regime into another. Studies on monolithic samples shows the mechanisms of damage in the Ti-8Al-1Er; specifically, that strain localization occurs near grain boundaries of high misorientation on the microscale and that twinning and dislocation density is concentrated near erbia strengthening particles (Er_2O_3) on the nanoscale.

15. SUBJECT TERMS

ICME; Additive manufacturing; Computational Material design; Titanium alloys

16. SECURITY CLASSIFICATION OF:			17. LIMITATION OF ABSTRACT	18. NUMBER OF PAGES	19a. NAME OF RESPONSIBLE PERSON
a. REPORT	b. ABSTRACT	c. THIS PAGE			STI Help Desk (email: help@sti.nasa.gov)
U	U	U	UU	33	**19b. TELEPHONE NUMBER** *(Include area code)* (757) 864-9658